Assessment of scale interactions associated with wake meandering using bispectral analysis methodologies

Dinesh Kumar Kinjangi and Daniel Foti[1]

Department of Mechanical Engineering, University of Memphis, Memphis, Tennessee, USA

Abstract

Large atmospheric boundary layer fluctuations and smaller turbine-scale vorticity dynamics are separately hypothesized to initiate the wind turbine wake meandering phenomenon, a coherent, dynamic, turbine-scale oscillation of the far wake. Triadic interactions, the mechanism of energy transfers between scales, manifest as triples of wavenumbers or frequencies and can be characterized through bispectral analyses. The bispectrum, which correlates the two frequencies to their sum, is calculated by two recently developed multi-dimensional modal decomposition methods: scale-specific energy transfer method and bispectral mode decomposition. Large-eddy simulation of a utility-scale wind turbine in an atmospheric boundary layer with a broad range of large length-scales is used to acquire instantaneous velocity snapshots. The bispectrum from both methods identifies prominent upwind and wake meandering interactions that create a broad range of energy scales including the wake meandering scale. The coherent kinetic energy associated with the interactions shows strong correlation between upwind scales and wake meandering.

Keywords: Wind turbine wake, Mode decomposition, Bispectral analysis

1. Introduction

Wind energy is derived from the kinetic energy available in the large-scale motions (> 1km) in the atmospheric boundary layer (ABL). However, the energy is harvested in the small surface sub-layer on the order of the scale of the turbine rotor (~ 100m), while the blades have length-scales that are only a fraction of that size (~ 1m). The disparate length-scales present around a wind turbine have been shown to have an effect on the formation and dynamic evolution of the wind turbine wake [1, 2, 3, 4] as well as effect the variability of power production [5]. New wind farms face substantial uncertainty in power production [6], and some developers [7] have been forced to lower estimates citing model inaccuracy. In order reduce the levelized cost of electricity to remain competitive compared to other power producers, wind farm models must become more accurate. The interactions among these disparate length-scales drive serious challenges to explain the turbulence mechanisms that transport energy and dynamics between the atmosphere and wind farms.

The genesis and evolution of wake meandering, a turbine-scale coherent oscillation of the wind turbine far wake, is still not understood. The wake motion affects wind turbines downstream in a wind farm [5], increases the variability of energy production [5], and has a negative influence on dynamic loading and aeroelasticity of downstream wind turbines [8, 9]. The stochastic meandering amplitude and wavelength play a particularly crucial role in the unsteady dynamics of wake recovery and wake interactions in wind farms [5]. The large ABL-scales [10] and the small turbine-scales [11] have been separately hypothesized to initiate the wake meandering phenomenon. However, it is not known what scale is dominant in producing wake meandering.

Velocity scale interactions are a consequence of the quadratic nonlinearity embedded in the momentum equation. This is commonly observed in the theory of the energy cascade, where energy transfers from energy-containing scales through the inertial sub-scale range and finally dissipated in the dissipation range. However, quadratic nonlinearity stipulates that scales interact in a triad of three wavenumbers or frequencies ($\boldsymbol{\kappa}_1, \boldsymbol{\kappa}_2$ and $\boldsymbol{\kappa}_3$ or f_1, f_2 and f_3) under the sum-zero condition: (e.g., $\boldsymbol{\kappa}_1 \pm \boldsymbol{\kappa}_2 \pm \boldsymbol{\kappa}_3 = 0$ or $f_1 \pm f_2 \pm f_3 = 0$) [12, 13]. Triadic interactions have been widely studied [14, 15, 16] as deviations from classical energy cascade. They can be used to understand nonlocality [17, 16], which can lead to events such as inverse cascade and extreme dissipation.

Assessment of triads can be accomplished through signal processing of a higher-order spectral analysis: the bispectrum, an analysis of quadratic phase coupling. While similar to the power spectrum, the second-order spectrum, the bispectrum is related to the skewness and is a function of two frequencies. It has been used to identify triadic interactions in high Reynolds number shear layers [18, 19, 20]. However, classical bispectrum signal processing analysis is only capable of detecting phase coupling in one-

[1]email: dvfoti@memphis.edu

dimensional signals.

Multi-dimensional analysis with large quantities of spatio-temporal data have become ubiquitous in fluid dynamics. A class of analyses that provides clear analysis and data reduction is modal decomposition. Flow variables are decomposed into the sum of the products of amplitude, temporal coefficient, and spatial mode. The most common approach is the method of snapshots [21], which uses an eigendecomposition of the covariance matrix to produce the proper orthogonal decomposition (POD). In wind energy, POD has been employed to assess coherent features [22, 23], which are based on orthogonality to optimally represent the variance of flow variables. Spectral analysis using dynamic mode decomposition [24], spectral POD [25] and Koopman mode decomposition [26] include analysis based on the frequency domain, which has been used to identify wind turbine wake features [2, 27, 28]. Recently, several modal decomposition analyses to assess scale interactions have been developed. Bispectral mode decomposition (BMD) was developed to extend classical bispectral analysis to multi-dimensional data [29]. A scale-specific energy transfer method (SSETM) [30] builds on DMD, the triple decomposition of velocity, and transport of kinetic energy to derive transport equations for scales and explicitly quantifies triadic interaction and their kinetic energy.

In this work, we assess the wake meandering scale and its interactions with upwind scales of a wind turbine. We compare the bispectrum and inter-related modal analyses produced by the BMD and SSETM with respect to wake meandering. Section 2 details the bispectral analysis related to BMD and SSETM. Section 3 discusses the numerical methods and computational details of the large-eddy simulation of a wind turbine. Section 4 discusses results of the bispectral analyses, and section 5 provides conclusions.

2. Bispectral Analysis

Triadic interactions arise from the quadratic nonlinearity in the Navier-Stokes equations. They are a triplet of wavenumbers or frequencies that sum to zero [13, 31]. The sum-zero condition for wavenumbers or frequencies is given by

$$\boldsymbol{\kappa}^l \pm \boldsymbol{\kappa}^m \pm \boldsymbol{\kappa}^n = 0, \qquad f^l \pm f^m \pm f^n = 0, \tag{1}$$

respectively, where we can consider both sum-interactions (e.g., $f^3 = f^1 + f^2$) and difference-interactions (e.g., $f^3 = f^1 - f^2$). For a random signal, power spectral density $\Phi_{uu}(f)$ is related to the autocorrelation function $R_{uu}(\tau) = E[u(t)u(t-\tau)]$, where $E[\cdot]$ is the expectation operator, through a Fourier transform as the following:

$$\Phi_{uu}(f) = \int_{-\infty}^{\infty} R_{uu}(\tau)\exp(-\mathrm{i}2\pi f\tau)\mathrm{d}\tau. \tag{2}$$

Analogously, the bispectral density is related to the third moment, $R_{uuu}(\tau_1,\tau_2) = E[u(t)u(t-\tau_1)u(t-\tau_2)]$, through a double Fourier transform of two frequencies:

$$\Phi_{uuu}(f_1,f_2) = \int_{-\infty}^{\infty}\int_{-\infty}^{\infty} R_{uuu}(\tau_1,\tau_2)\times \exp(-\mathrm{i}2\pi(f_1\tau_1+f_2\tau_2))\mathrm{d}\tau_1\mathrm{d}\tau_2. \tag{3}$$

The bispectral density is composed of two frequencies, correlates those frequencies to their sum, and can detect the triadic interactions of the frequencies. Similar to the power spectral density, the bispectral density can be defined in terms of the expectation of Fourier modes $\hat{u}(f)$ as follows:

$$\Phi_{uuu}(f_1,f_2) = \lim_{T\to\infty}\frac{1}{T}E[\hat{u}(f_1)^*\hat{u}(f_2)^*\hat{u}(f_1+f_2)]. \tag{4}$$

The bispectrum is a hexagonal region that is function of the two frequencies and is restricted by the Nyquist frequency f_N. The principal region corresponds to sum-interactions and the conjugate region corresponds to difference-interactions. All other regions due to symmetry contain only redundant information.

We detail the two recently developed methods employed in the work herein to assess triadic interactions based on mode decompositions of the velocity variables. Both methods quantify a bispectrum based on two frequencies and enforces the triadic sum-zero condition.

2.1. Scale-specific Energy Transfer Method

The method is built on the assumption that coherent turbulent fluctuations can be related to a specific frequency scale. In particular, the method employs the triple decomposition of the spatio-temporally varying velocity variable ($\boldsymbol{u}(\boldsymbol{x},t)$) into mean ($\boldsymbol{U}(\boldsymbol{x})$), coherent ($\tilde{\boldsymbol{u}}(\boldsymbol{x},t)$), and random ($\boldsymbol{u}''(\boldsymbol{x},t)$) components, which is given by the following: $\boldsymbol{u}(\boldsymbol{x},t) = \boldsymbol{U}(\boldsymbol{x}) + \tilde{\boldsymbol{u}}(\boldsymbol{x},t) + \boldsymbol{u}''(\boldsymbol{x},t)$. Triple decomposition requires criteria to separate the three components. The mean velocity can be extracted via time averaging; however, that does not provide enough information to separate the coherent and random signals. Additionally in this method, the coherent velocity will be decomposed into R coherent velocities identified by a specific discrete frequency scale. We consider our data to be a matrix of columns of the instantaneous snapshots of the velocity flow field.

Mode decomposition is tasked to separate the coherent velocity from the random velocity and separate the coherent velocity into a series of scale-specific coherent velocities. The mode decomposition of the velocity employs dynamic mode decomposition (DMD), which is a linear approximation of the Koopman operator. The first aspect of DMD is singular value regularization, which projects the fluctuating velocity (velocity minus the mean velocity) into POD modes. Typically, only a percentage (in most cases $> 90\%$) of the total accumulated energy of the POD modes are retained. DMD proceeds to decompose the flow field based on discrete frequencies. Each mode is associated with a discrete frequency based on the spectral characteristics of linear discrete dynamical system of

$\boldsymbol{u}_{i+1} = A\boldsymbol{u}_i$, where $\boldsymbol{u}_i$ is the ith time snapshot of the multi-dimensional velocity field and A is the approximate linear operator. The scale-specific coherent velocity is quantified by the product:

$$\tilde{\boldsymbol{u}}^l = \boldsymbol{\phi}^l \alpha^l \mu^l, \tag{5}$$

where a scalar amplitude α^l, complex temporal coefficient $\mu^l(t) = \mathrm{i}\mu_i^l + \mu_r^l = \mathrm{e}^{\lambda^l t}$, and spatial mode $\boldsymbol{\phi}^l(\boldsymbol{x})$ are computed by DMD. The eigenvalue, λ^l, is associated with a specific time or frequency scale. The summation of R modes gives the coherent velocity

$$\tilde{\boldsymbol{u}} = \sum_{l=0}^{R} \tilde{\boldsymbol{u}}^l. \tag{6}$$

Using a sparsity-promoting DMD [32], a final R number of modes are selected. These R modes are used to directly calculate the scale-specific coherent velocity. The random velocity is obtained from the difference of the total velocity and sum of mean and coherent velocity.

The scale-specific coherent kinetic energy (CKE) associated with the velocity of two scales is obtained by the inner product of the lth and mth coherent velocities

$$\tilde{k}^{l,m} = \frac{1}{2}\overline{\tilde{\boldsymbol{u}}^l \cdot \tilde{\boldsymbol{u}}^{m*}} = \frac{1}{2}\overline{\mu^l \mu^{m*}} \alpha^l \alpha^m \left(\boldsymbol{\phi}^l \cdot \boldsymbol{\phi}^{m*}\right), \tag{7}$$

where $*$ is the complex conjugate and $\bar{\cdot}$ averaging is temporal averaging.

The sum-zero condition of triadic interactions is implied in scale-specific CKE through the product of temporal components: $\mu^l \mu^{m*} = \exp[(\lambda^l + \lambda^{m*})t] = \exp[\lambda^n t]$, a sum-interaction. Using the condition, the scale-specific CKE can be summed over all triads to obtain the summed scale-specific CKE of one scale

$$\tilde{k}^l = \sum_{l=\pm m \pm n} \tilde{k}^{m,n}. \tag{8}$$

Finally, the total CKE is obtained by summing over all combinations as follows

$$\tilde{k} = \sum_l \tilde{k}^l = \sum_l \sum_{l=\pm m \pm n} \overline{\tilde{k}}^{m,n}. \tag{9}$$

This method quantifies the kinetic energy associated with triadic interactions. Following Ref. [30], the transport of scale-specific CKE and the interscale transfer can be quantified. Here, the focus will be on the kinetic energy associated with the scales to quantify the bispectrum of dominant coherent scales.

2.2. Bispectral Mode Decomposition

The bispectral mode decomposition is a relatively new method that inherits properties of the bispectral density for multi-dimensional data. Triadic interactions are embedded directly as the method correlates two frequencies to their sum. As described in Ref. [29], the method adapts Welch's method to calculate an ensemble average over realizations with the Fourier transforms. For brevity, we will not re-derive the entire method herein, but detail the important aspects that will be employed in the analysis. Similar to SSETM, we start with a series of snapshots of the instantaneous velocity flowfield $\boldsymbol{u}(\boldsymbol{x}, t)$. The discrete Fourier transform at the lth frequency is given by $\hat{\boldsymbol{u}}_l = \hat{\boldsymbol{u}}(\boldsymbol{x}, f_l)$ and the element-wise product of two transforms is given by $\hat{\boldsymbol{u}}_{l\circ m} = \hat{\boldsymbol{u}}(\boldsymbol{x}, f_l) \circ \hat{\boldsymbol{u}}(\boldsymbol{x}, f_m)$, where $\circ$ is the element-wise product. Using the Welch's like method, N_{blk} realization of the Fourier transform of are obtained, $\hat{\boldsymbol{u}}^1(\boldsymbol{x}, f_l), \hat{\boldsymbol{u}}^2(\boldsymbol{x}, f_l), \ldots \hat{\boldsymbol{u}}^{N_{\mathrm{blk}}}(\boldsymbol{x}, f_l)$, where superscript indicates realization.

The bispectral decomposition is similarly computed to the bispectral density in Eq. (4) by defining an integral measure of the point-wise bispectral density as

$$\begin{aligned} b(f_l, f_m) &\equiv E\left[\int_{\Omega} \hat{\boldsymbol{u}}_l^* \circ \hat{\boldsymbol{u}}_m^* \circ \hat{\boldsymbol{u}}_{l+m} d\boldsymbol{x}\right] \\ &= E[\hat{\boldsymbol{u}}_{l\circ m}^H \boldsymbol{W} \hat{\boldsymbol{u}}_{l+m}], \end{aligned} \tag{10}$$

where $*$ is the complex conjugate, H is the complex conjugate transpose, $\boldsymbol{W}$ is a diagonal matrix of spatial quadrature weights and Ω is the spatial domain of the flow.

Similar to other mode decompositions, modes are related to expansions. Two linear expansions with coefficients a_{ij} accounting for the interaction of the two frequencies, $\hat{\boldsymbol{u}}_{l\circ m}$ or cross-frequency field, and outcome, $\hat{\boldsymbol{u}}_{l+m}$ or bispectral modes, as follows

$$\boldsymbol{\phi}_{l\circ m}^i = \sum_{j=1}^{N_{\mathrm{blk}}} a_{ij}(f_{l+m}) \hat{\boldsymbol{u}}_{l\circ m}^j = \hat{\boldsymbol{U}}_{l\circ m} \boldsymbol{a}_i \tag{11}$$

$$\boldsymbol{\phi}_{l+m}^i = \sum_{j=1}^{N_{\mathrm{blk}}} a_{ij}(f_{l+m}) \hat{\boldsymbol{u}}_{l+m}^j = \hat{\boldsymbol{U}}_{l+m} \boldsymbol{a}_i, \tag{12}$$

where $\hat{\boldsymbol{U}}_{l\circ m}$ and $\hat{\boldsymbol{U}}_{l+m}$ are data matrices made of column vectors of $\hat{\boldsymbol{u}}_{l\circ m}^j$ and $\hat{\boldsymbol{u}}_{l+m}^j$, respectively, and $\boldsymbol{a}_i = [a_{i1}(f_{l+m}), a_{i1}(f_{l+m}), \ldots, a_{iN_{\mathrm{blk}}}(f_{l+m})]^T$ is the i-th vector of expansion coefficients for the lth and mth frequency pair. The goal is the find the values of $a_{ij}(f_{l+m})$ that maximize the absolute value of $b(f_l, f_m)$ in Eq. (10). The optimal coefficients $\boldsymbol{a}_1$ are found on the unit vector $\|\boldsymbol{a}_1\| = 1$, which reduce the optimization to

$$\boldsymbol{a}_1 = \arg\max \left|\frac{\boldsymbol{a}^H \boldsymbol{B} \boldsymbol{a}}{\boldsymbol{a}^H \boldsymbol{a}}\right|, \tag{13}$$

where $\boldsymbol{B}$ is the weighted bispectral density matrix and is given as

$$\boldsymbol{B} = \frac{1}{N_{\mathrm{blk}}} \hat{\boldsymbol{U}}_{l\circ m}^H \boldsymbol{W} \hat{\boldsymbol{U}}_{l+m}. \tag{14}$$

The optimization problem entails finding the vector that maximizes the Rayleigh quotient of $\boldsymbol{B}$. The numerical range of the set of all Rayleigh quotients is

$$F(\boldsymbol{B}) = \frac{\boldsymbol{a}^H \boldsymbol{B} \boldsymbol{a}}{\boldsymbol{a}^H \boldsymbol{a}}, \tag{15}$$

where the largest absolute value of the numerical range is defined as the numerical radius

$$r(\boldsymbol{B}) = \max|\lambda| : \lambda \in F(\boldsymbol{B}),$$
$$= \max\left|\frac{\boldsymbol{a}_1^H \boldsymbol{B} \boldsymbol{a}_1}{\boldsymbol{a}_1^H \boldsymbol{a}_1}\right| \tag{16}$$

where λ are the eigenvalues of $F(\boldsymbol{B})$. Hence, the optimization problem is tasked to find the numerical radius, largest eigenvalue, of the Rayleigh quotient. The numerical radius, referred to as the complex mode bispectrum λ_1, is given as

$$\lambda_1 = \left|\frac{\boldsymbol{a}_\mathbf{1}^H \boldsymbol{B} \boldsymbol{a}_\mathbf{1}}{\boldsymbol{a}_\mathbf{1}^H \boldsymbol{a}_\mathbf{1}}\right|. \tag{17}$$

We follow the algorithm in Ref. [29], which employs the method of He and Watson [33].

3. Large-eddy Simulations

We employ the Virtual Flow Simulator (VFS-Wind)[34] for large-eddy simulations. The incompressible, spatially-filtered continuity and momentum equations in generalized curvilinear coordinates [35] are formulated as follows in index notation where indices $i, j, k, l = 1, 2, 3$ and repeated indices imply summation:

$$J\frac{\partial U^i}{\partial \xi^i} = 0, \tag{18}$$

$$\frac{1}{J}\frac{\partial U^i}{\partial t} = \frac{\xi_l^i}{J}\left(-\frac{\partial}{\partial \xi^j}(U^j u_l) + \frac{\mu}{\rho}\frac{\partial}{\partial \xi^j}\left(\frac{g^{jk}}{J}\frac{\partial u_l}{\partial \xi^k}\right) - \frac{1}{\rho}\frac{\partial}{\partial \xi^j}\left(\frac{\xi_l^j p}{J}\right) - \frac{1}{\rho}\frac{\partial \tau_{lj}}{\partial \xi^j}\right), \tag{19}$$

where ξ^i are the curvilinear coordinates, $\xi_l^i = \partial\xi^i/\partial x_l$ are the transformation metrics, J is the Jacobian of the geometric transformation, u_i is the i-th component of the velocity vector in Cartesian coordinates, $U^i{=}(\xi_m^i/J)u_m$ is the contravariant volume flux, $g^{jk} = \xi_l^j \xi_l^k$ are the components of the contravariant metric tensor, ρ is the density, μ is the dynamic viscosity, p is the pressure, and τ_{ij} represents the anisotropic part of the subgrid-scale stress tensor. The closure for τ_{ij} is provided by a dynamic Smagorinsky model [36, 37]

$$\tau_{ij} - \frac{1}{3}\tau_{kk}\delta_{ij} = -2\rho\nu_t \widetilde{S}_{ij}, \tag{20}$$

where the $\widetilde{(\cdot)}$ denotes the grid filtering operation, ρ is the density, and $\widetilde{S}_{ij}$ is the filtered strain-rate tensor. The sub-grid scale (SGS) eddy viscosity ν_t is given by

$$\nu_t = C_s \varDelta^2 |\tilde{S}|, \tag{21}$$

where C_s is a dynamic Smagorinsky coefficient [38], $\varDelta$ is the filter size taken as the cubic root of the cell volume, and $|\tilde{S}| = (2\widetilde{S}_{ij}\,\widetilde{S}_{ij})^{\frac{1}{2}}$.

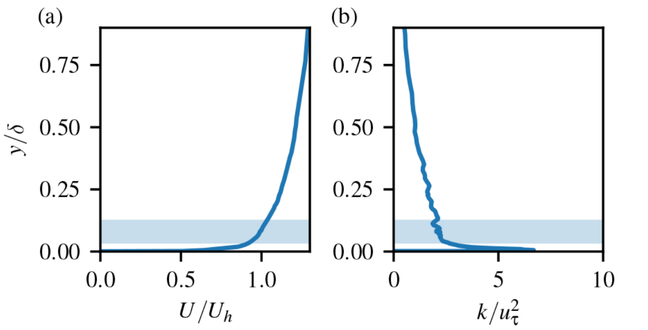

Figure 1: The upwind (a) mean streamwise velocity normalized by the turbine hub height velocity, U_h and (b) turbulence kinetic energy normalized by the upwind friction velocity, u_τ. The blue shaded region shows the extent of the turbine rotor.

The forces exerted by the wind turbine are parameterized by an actuator surface model [39]. The blade is represented by a two-dimensional discretized surface along the chord and radial directions where the forces are determined using a blade element method based on tabulated blade twist angle and chord length. The lift $\boldsymbol{L} = \frac{1}{2}\rho C_L c|\boldsymbol{V}_{rel}|^2\boldsymbol{n}_L$ and drag $\boldsymbol{D} = \frac{1}{2}\rho C_D c|\boldsymbol{V}_{rel}|^2\boldsymbol{n}_D$, where C_L and C_D are tabulated lift and drag coefficients at angle of attack, c is the blade chord, $\boldsymbol{V}_{rel}$ is the relative incoming velocity, and $\boldsymbol{n}_L$ and $\boldsymbol{n}_D$ are the unit vectors in the directions of lift and drag, respectively. The relative incoming velocity $\boldsymbol{V}_{rel} = u_x(\boldsymbol{X}_{LE})\boldsymbol{e}_x + (u_\theta(\boldsymbol{X}_{LE}) - \varOmega r)\boldsymbol{e}_\theta$, where $\boldsymbol{X}_{LE}$ represents the leading edge coordinates of the blade, $\varOmega$ is the rotational speed of the rotor, $\boldsymbol{e}_x$ and $\boldsymbol{e}_\theta$ are the unit vectors in the axial flow and rotor rotating directions, respectively. A smoothed discrete delta function [40] is employed to interpolate the background velocity to the blade. Stall delay model [41] and the tip-loss correction [42] are employed to take into account the three-dimensional effects.

A model for the nacelle [43] is used to represent the nacelle geometry by the actual surface of the nacelle with distributed forces decomposed into two parts, the normal component and the tangential component. The normal component of the force is computed in a way to satisfy the non-penetration condition, which is similar to the direct forcing immersed boundary methods [44]. The tangential forces are based on the incoming velocity and an empirical friction coefficient [45].

We undertake a large-eddy simulation of a single wind turbine to resemble the Clipper Liberty C96 2.5 MW turbine [46, 47], with a diameter $D = 96$ m and hub height $H = 80$ m. A constant tip-speed ratio $\lambda = \dot{\theta}D/2U_h = 8.0$, where $\dot{\theta}$ is the angular velocity and U_h is the hub height velocity, is enforced. A precursory simulation of a boundary layer inflow is performed to provide an instantaneous incoming velocity resembling an atmospheric boundary layer. The domain of $(L_x \times L_y \times L_z) = (120\delta \times \delta \times 6\delta)$, where δ is the boundary layer height, discretized with a uniform mesh in the vertical direction of $\delta/\Delta_y = 200$ and in the streamwise and spanwise by $\delta/\Delta_x = 30$. Figure 1 shows the mean streamwise velocity profile and the turbulence kinetic energy, which shows strong velocity and kinetic energy gradients across the turbine rotor. The precursory simulation is used to resolve a broad range of upwind length scales including long and very long coherent structures, spanwise features that appear in boundary layers [48, 49], which have been hypothesized have an effect on wind turbine wake meandering. These features are typically $2\delta - 10\delta$ long. The Reynolds number based on the boundary layer bulk velocity $Re_b = U_b\delta/\nu = 6.6 \times 10^8$ and friction velocity and hub height $Re_\tau = u_\tau H/\nu = 2.5 \times 10^6$.

The computational domain of the primary wind turbine $(L_x \times L_y \times L_z) = (14D \times \delta \times 6D)$ is discretized in a Cartesian grid $(N_x \times N_y \times N_z) = (500 \times 150 \times 200)$, where a uniform grid with space of $D/50$ is located in a $2D$ cubic box around the turbine blades. The grid is then stretched towards the domain boundaries. The turbine is positioned $2D$ downwind of the inflow at the center of the $y - z$ plane and provides buffer region to allow the inflow from the precursory simulation to relax to the finer primary turbine grid. Instantaneous velocity planes from the precursory simulation are interpolated to the primary grid locations at the inflow at every time step. Free-slip boundary conditions are imposed in the top $(+y)$ and spanwise $(\pm z)$ directions, while the bottom wall $(-y)$ is a no-slip condition with a wall model. For validation of the numerical methods of this turbine and grid spacing, please see Ref. [47].

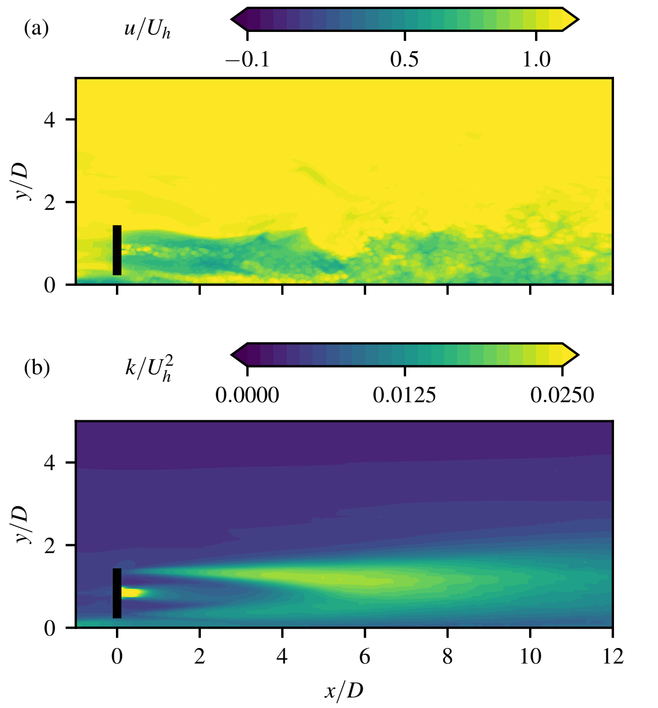

Figure 2: Contours of the centerline plane of the (a) instantaneous streamwise velocity u and (b) turbulence kinetic energy k normalized by the mean hub height velocity.

4. Results

The instantaneous streamwise velocity in the wake of the wind turbine is shown in Fig. 2(a). Several coherent features are readily apparent, including the large velocity deficit that forms behind the wind turbine and the inner wake that forms due to the nacelle at the center of the rotor. Both persist for several diameters downwind as the inner wake expands into the outer wake formed by the velocity deficit. Within three diameters downwind, the motions of wake meandering become evident with an oscillation of the velocity deficit in the vertical direction. Due to the strong turbulence in the incoming boundary layer flow, and the influence of the wall downwind of the turbine, the coherent velocity deficit collapses. Wake meandering is present in the far wake at $x/D > 6$, albeit more obvious in the spanwise direction (see Ref. [47]), as the periodic oscillation will convect downwind.

The turbulence kinetic energy (TKE) at the centerline plane, as shown in Fig. 2(b), shows the strong fluctuations behind the nacelle and at the tip position, similar to Refs. [3, 27, 50, 51, 46]. As the inner and outer wake close to the rotor evolve, the TKE spreads. Around $x/D = 5$, the maximum TKE in the far wake is co-located where wake meandering begins to appear in Fig. 2(a). Wake meandering increases the variations in the velocity as strong periodic motions appear. The high TKE in the far wake persists downstream to mark the region where the wake meanders. The convergence of the statistics of the velocity, including the mean, variance, and skewness, are described in Appendix A.

The pre-multiplied spectra of the transverse fluctuating velocity $f\Phi_{ww}$ upwind and at various locations downwind are shown in Fig. 3(a) at the blade midpoint above the centerline, $y = H + D/4$ to capture signatures of both tip- and hub-located coherent structures. The transverse velocity is employed due to the strong spanwise regular fluctuations due to wake meandering. From the spectra, we can identify important frequency modes, in terms of Strouhal number normalized by the U_h and D, in the flow pertaining to the wake meandering. In the wind turbine wake, these are the characteristics scales. Starting with the upwind position at $x/D = -2$, the spectrum peaks broadly and flatly around $St \approx 0.2 - 0.4$, and quickly decreases. Note that for the upwind turbulence boundary, D and U_h are the not characteristic scales, the distance from the wall H and the friction velocity are characteristic scales, prominent scales on the pre-multiplied (compensated) spectrum are shifted to the left for the upwind location due to the scaling. In the low frequency range under $St < 0.2$, about a decade of the frequency range scales with f and is dynamically important to incoming flow. Two frequencies in the range as labeled in

Fig. 3(a), $St_{l1} = 0.06$ and $St_{l2} = 0.12$ have relatively higher energy locally. The peaks are related to the long and very long coherent structures that appear in turbulent boundary layers [49, 48]. The precursory simulation was specifically designed to capture these long physical features. The location of the turbine is within the lower 10% of the boundary layer (inner region) and located in the log-layer. Spectral peaks at St_{l1} and St_{l2} correspond well to peaks identified in Ref. [52] in the log-layer with a non-dimensional frequency $f\delta/U_\infty = 5$ and 10. The effects of these frequencies will be explored below. Aft of the wind turbine, the range of peak frequencies spans from $0.1 < St < 3$, before energy decreases. The turbulence produced by the wind turbine add markedly more fluctuations to the wake over this broad range. At the closest location to the rotor plane of $x/D = 1$, a peak around hub vortex frequency $St = St_h = 0.55$ is consistent with the previous studies [47, 53] and the frequency of the rotor rotation $St_r = D/(TU_h) = 2.5$, where T is the period of rotation, clearly appear. Both the hub vortex and the tip vortices quickly dissipate downwind. The energy modes at $x/D = 2$ are similar, but the effect of the hub vortex is slightly diminished compared to closer to the rotor plane. This is due to the expansion of the inner shear layer as discussed in Fig. 2(b). A dominate frequency around the wake meandering frequency $St_w \approx 0.15$ is present downwind at locations $x/D = 4$ and 6. This is consistent with a long list of published studies [11, 54, 55, 56, 57, 3, 47, 27]. In comparison to the spectra at $x/D = -2$, no spectra in the wake demonstrates high energy at St_{l1} or St_{l2}. However, all have similar energy ranges around the wake meandering frequency. This will be explored further below.

Figure 3(b) shows contours of the pre-multiplied spectrum of the streamwise velocity $f\Phi_{uu}$ along the centerline at hub height. Both the wake meandering and hub vortex modes appear at the hub height. Additional peaks appear for frequencies greater and less than wake meandering frequency. A peak, that can also be observed in Fig. 3(a) at $St = 0.3$ can be related to wake meandering as the first harmonic of the periodic oscillation ($2\,St_w$). This frequency mode continues far downstream, but does not appear until $x/D > 5$, where wake meandering has commenced. Additional very low frequencies could be related to spectral energy in the incoming flow that is modulated by the wind turbine. From the centerline at hub height, it is difficult to observe any modes related to the rotor rotation.

Next, we focus on the calculation of the bispectrum and start with examining the results of DMD, which is used to calculate the bispectrum and scale-specific kinetic energy for SSETM. Furthermore, DMD provides an alternative method to identify dominant modes based on frequency. We employ the DMD algorithm that projects the snapshot matrix into POD modes for dimensionality reduction and elimination of some spurious modes. The snapshot matrix is populated with slices of the three-dimensional velocity vector on the $x-y$ centerline plane. The constant time

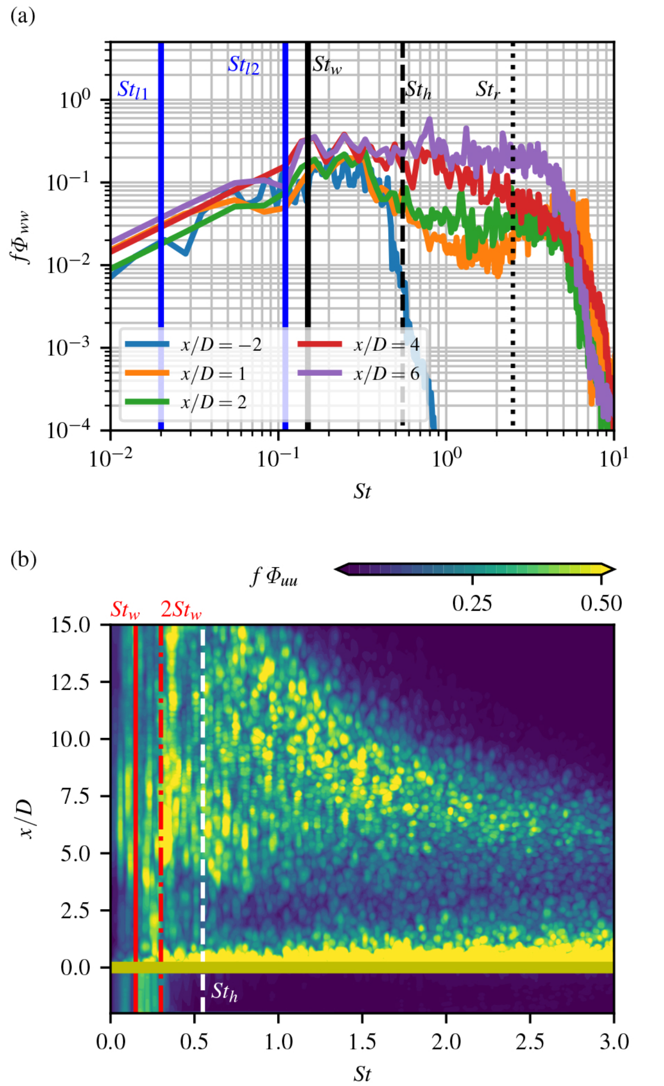

Figure 3: (a) Pre-mulitplied power spectral density of the transverse velocity $f\Phi_{ww}$ at locations $x/D = -2, 1, 2, 4$ and 6 at $y = H + D/4$ (vertical lines indicate St_{l1}, St_{l2} St_w, St_h, and St_r) and (b) contours of the pre-mulitplied power spectral density of the streamwise velocity $f\Phi_{uu}$ at the hub height $y = H$. (vertical lines indicate St_w, $2\,St_w$, and St_h).

step between each snapshot is $T/30$ and a total of 10,000 snapshots where collected. The mode decomposition is performed on the largest POD modes, which has the accumulated energy corresponding to 90% of the total TKE in the flow. Based on previous analyses in Refs. [27, 53], TKE associated with wake meandering and hub vortex is expected to make up a large fraction of the total TKE and be identified as one of the most amplified dynamic modes. The total number of dynamic modes that are identified in the top 90% of TKE is $R = 990$. A sparse sampling algorithm [32] is utilized to identify the most important modes based on the criterion of an L1 error minimization of the selected modes and the full POD space. Two additional selections are identified $R = 775$ and $R = 492$, where the error residual increases with fewer selected modes.

Figure 4 shows the spectra of the DMD frequency and normalized DMD amplitude of three selected mode set. The frequency is obtained from the imaginary part of the Ritz values μ_i, the spectra component of the DMD tuple, as $St = \mathcal{I}(\ln \mu_i)/\Delta t(D/U_h)$. As the number of modes selected decreases fewer modes at higher frequencies as well as some lower frequencies are selected. From Fig. 4, it is most obvious that the large frequency modes up to $St \approx 2.5$ are removed by sparse sampling. Modes with frequencies higher than this value, including modes related to the rotor frequency are not identified based on the coherence in the top 90% of the TKE, suggesting that the energy related the tip vortices is relatively small compared to the overall wake and atmospheric boundary layer flow. The highest amplitudes are located near the same frequency range shown in the pre-multiplied spectra in Fig. 3, where the highest amplitude is related to wake meandering. In fact, the highest amplitude is associated with the frequency of $St = St_w$. Other high amplitudes are associated with lower frequencies of the incoming flow as well. Furthermore, DMD is able to identify the hub vortex mode as well, but it is not present in the smallest sparse sampling set of $R = 493$.

The bispectrum as computed for SSETM is the relationship between scales quantified by the magnitude of the correlation of the amplitudes and temporal (spectral) coefficients: $\overline{\alpha^l \mu^l \alpha^m \mu^m}$. The triadic non-zero conditions are explicitly imposed by the relationship:

$$\begin{aligned} \mu^l \mu^m &= \exp(i2\pi f^l t/\Delta t)\exp(\mathrm{i}2\pi f^m t/\Delta t) \\ &= \exp(\mathrm{i}2\pi(f^l + f^m)t/\Delta t). \end{aligned} \tag{22}$$

The natural log of the coefficient, $\ln \overline{\alpha^l \mu^l \alpha^m \mu^m}$, is shown in Fig. 5(a), 5(b), and 5(c), where Fig. 5(b) zooms in on the important difference-interactions at low frequencies and Fig. 5(c) zooms in on the important sum-interactions at low frequencies. In Fig. 5(a), the bispectrum of all modes computed from DMD modes are shown for the sum-interactions and the difference-interactions. Note that all other quadrants of the bispectrum contain redundant data and only these two triangular regions are required to observe the entire bispectrum. The bispectrum is also bounded

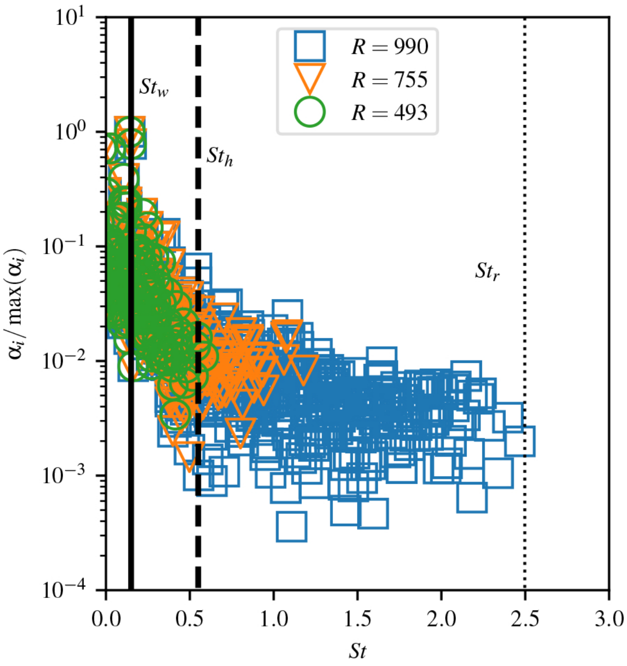

Figure 4: DMD amplitudes $|\alpha_i|/\max(\alpha)$ and positive St for different sparse sampling levels. Vertical lines indicate St_w, St_h, and St_r

by the Nyquist limit, which is $St_s = 15$, to create a quadrilateral region instead of a triangular region; however, the frequencies obtained from DMD and those that are important to this analysis are much lower than the Nyquist frequency. The convergence of the bispectrum is discussed in Appendix A.

Figure 5(a) also shows the outline of the bispectrum that is created by reducing the number of modes selected. As the number of modes is reduced, more are concentrated near the lower frequencies. At higher frequencies, only select frequency interactions are identified. Bands of high bispectral coefficient are observed running at constant St^l or St^m. The higher bands as well as diagonal bands are observed at lower frequencies $St^l, St^m < 1$. There are some differences between the sum-interactions and the difference-interactions around $St^l = \pm 0.15$ as shown in Fig. 5(b). The bispectral coefficient is higher for the sum-interactions compared to the difference-interactions in the low frequencies. This is an indication that around the wake meandering frequency, it is more prevalent for modes to interact and form higher frequency modes. Some of the dominant difference-interactions are highlighted in Fig. 5(b). These include the wake meandering self-interaction, where the third frequency in the triad is the mean flow distortion. This shows the prominence of interactions to add to CKE in the zero frequency. There are also interactions with other low frequencies including the upwind frequencies.

Prominent sum-interactions are highlighted in Fig. 5(c). In this view, the sum-interactions between the wake meandering modes and other dominant scales can be identified.

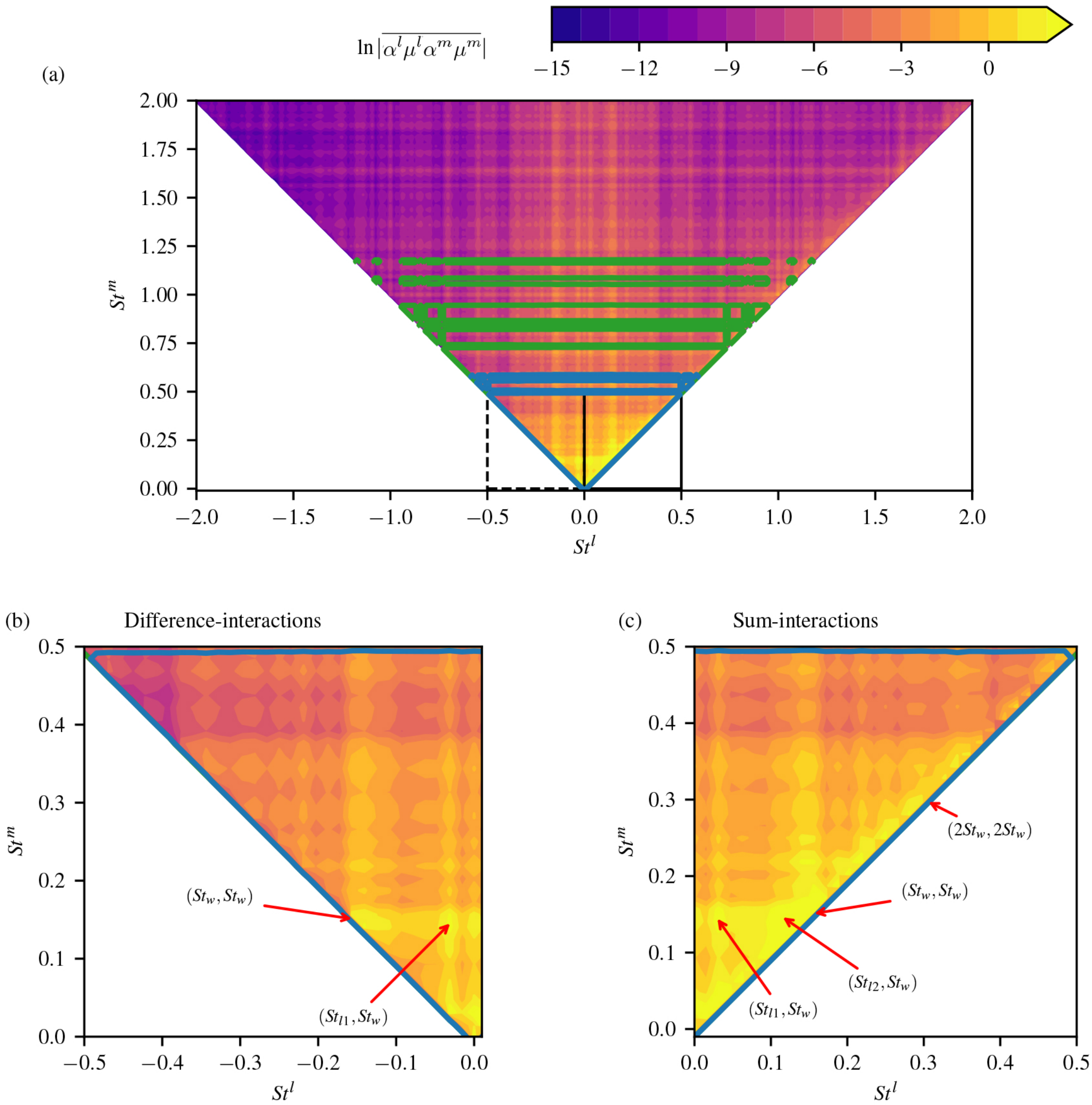

Figure 5: (a) Magnitude of the bispectral correlation for SSETM for $R = 990$. Contour lines outlines all selected scales for $R = 755$ (green) and $R = 493$ (blue). (b) Zoom-in to dashed squared outlined area showing difference-interactions on (a). (c) Zoom-in to solid squared outlined area showing sum-interactions on (a)

The wake meandering mode interacts strongly with itself and the first harmonic interacts with itself. Additionally, we identify interactions with wake meandering from the lower frequency signals highlighted in the upwind spectrum at $x/D = -2$ in Fig. 3(a). The bispectral coefficients of these sum-interactions are high and suggest that upwind flow features interact with downwind wake meandering. These produce energy at new frequencies that are unrelated to both wake meandering and the incoming flow.

The BMD is performed on the same snapshot matrix described above and employed for the SSETM with DMD. Because it is similar to Welch's method, BMD splits the snapshot matrix into several overlapping segments of $N = 2^{11}$, with an overlap of $N/2$. This is the same segmentation used for the spectral power density shown in Fig. 3(b), which also is produced from the same snapshots, for consistency. The convergence of the bispectrum is discussed in Appendix A. The mode bispectrum λ_1 is calculated for the sum-interaction and difference-interaction regions as shown in Fig. 6(a). The bispectrum of BMD is both similar and different in comparison to the SSETM bispectrum. First, the frequency range is significantly different as BMD captures discrete frequencies from the lowest range to the Nyquist frequency. The top bound of the bispectrum region is based on the Nyquist frequency of the data acquisition St_s. Figure 6(a) shows high correlation in the lowest frequency ranges, similar to Fig. 5(a), but interactions at $St^l = 0 = St_0$ are especially high. Additionally, there are two strong interaction regions that exist, which are not identified with SSETM, these are the interactions with the rotor frequency, specifically, the blade frequency $St_b = 3\,St_r$, which is shown in Fig. 6(b). One region is designated with interactions with the low frequencies, including St_0 and the wake meandering frequency, St_w. The second region is the self-interaction of the blade frequency with itself. The bispectra of higher harmonics of the blade frequency are relatively lower and are not readily identifiable in Fig. 6(a).

Figure 6(c) shows the low frequency region of the difference-interactions, similar to the focus in Fig. 5(b). There are several peaks that corresponds to the wake meandering frequency and its harmonic. These locations are difference-interactions that total to a third frequency of zero, the mean flow distortion. Similar to SSETM, BMD captures these interactions. Figure 6(d) focuses on the dominant low frequency region of the sum-interactions. Peaks in the bispectrum appear at each of the same locations as seen in Fig. 5(c), including the incoming low frequency scales, the wake meandering scale and the first harmonic of the wake meandering scale. The relative peaks compared to the other frequency pairs are similar to the SSETM bispectrum. This is an additional confirmation that these scales are dominant and identified by several different methodologies. Additionally, the bispectrum is higher along the constant St_w lines, indicating that many scales interact with the bispectrum. As the frequencies approach St_0, the bispectrum increases to its highest value. This is slightly different than the SSETM bispectrum where the wake meandering self-interaction is the highest value. The BMD method produces a higher resolution of frequencies compared to the SSETM. Nevertheless, both methods produce a similar bispectrum that can be used to investigate how scales interact. However, one interesting observation is the difference in the relative magnitude of the difference-interactions to the sum-interactions between the two methods. BMD shows much stronger difference-interactions at low frequencies over a larger range than the sum-interactions. SSETM does not capture the same differences.

Next, we look at the spatial distribution of how select, dominant scales interact with each other starting with the kinetic energy identified from the SSETM. Figure 7 shows the scale-specific CKE of the interactions between the wake meandering scale and three other scales: mean (St_0), upwind (St_{l1}), and first harmonic of wake meandering ($2\,St_w$). In SSETM, the CKE attributed to the interaction of two scales is explicitly calculated. First, the interaction of wake meandering with the mean flow distortion is quantified. Note that based on the sum-zero condition, the sum-interaction of these two scales adds to kinetic energy in the wake meandering scale. In other words, the CKE in this interaction is a portion of the total wake meandering CKE. Strong interactions occur in the wake shear layer at the top and the bottom in the far wake after $x/D > 2$. However, there is little interaction between the scales along the centerline. Wake meandering in the vertical direction is significantly affected by the presence of the wall and the high shear in the wall boundary layer formed by the recovering wake and the wall. The vertical wake meandering amplitude is attenuated in the far wake with larger attenuation with increased distance from the turbine. The turbulent scales in the wall boundary layer for this analysis are not coherent so there is no scale associated with it. The effects on the wake meandering are captured by this triad of the interaction of wake meandering and mean flow distortion. Similarly, the shear layer of the mean flow above the turbine has an increased interaction with wake meandering, but is not as strong as there are upwind scales that also contribute to the kinetic at this location. The interaction between the upwind scale and wake meandering in Fig. 7(b) shows that the interaction of these two modes has highest energy in the far wake in $x/D > 6$, which suggests that wake meandering is augmented by upwind energy far downwind. This sum-interaction produces a scale at a new frequency slightly larger than the wake meandering frequency that could explain the broadness of the power spectral density in Fig. 3(a) and 3(b) around the wake meandering frequency peak. Finally, Fig. 7(c) shows the difference-interaction of the first harmonic of the wake meandering and the wake meandering scale. These sum to the wake meandering scale. The CKE in this interaction is relatively small compared to the other examples shown. This suggests that energy does not transfer to the wake meandering scale from higher

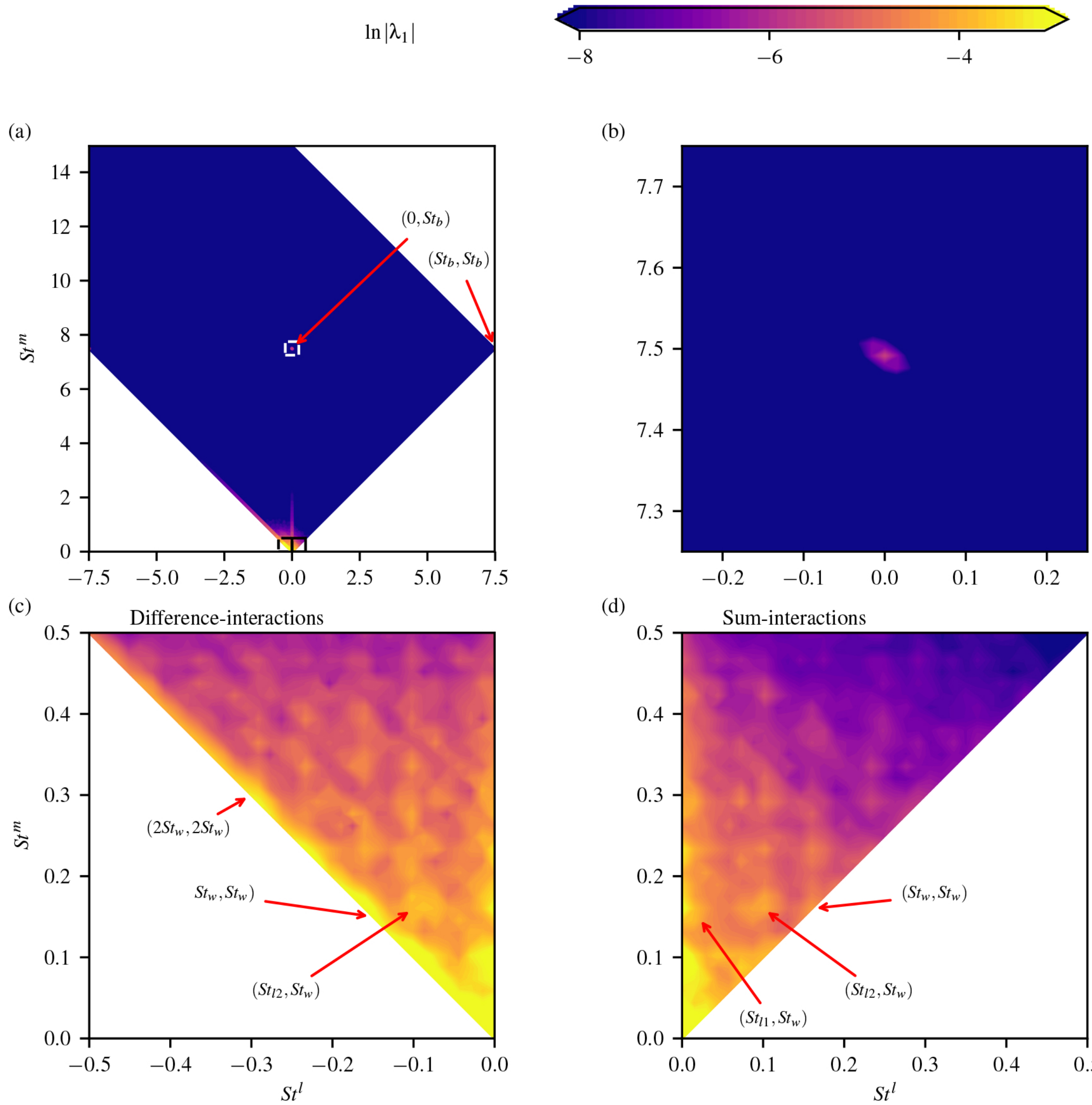

Figure 6: (a) Magnitude of the BMD. (b) Zoom-in to white dashed squared outlined area on (a). (c) Zoom-in to black dashed squared outlined area on (a). (d) Zoom-in to solid squared outlined area on (a),

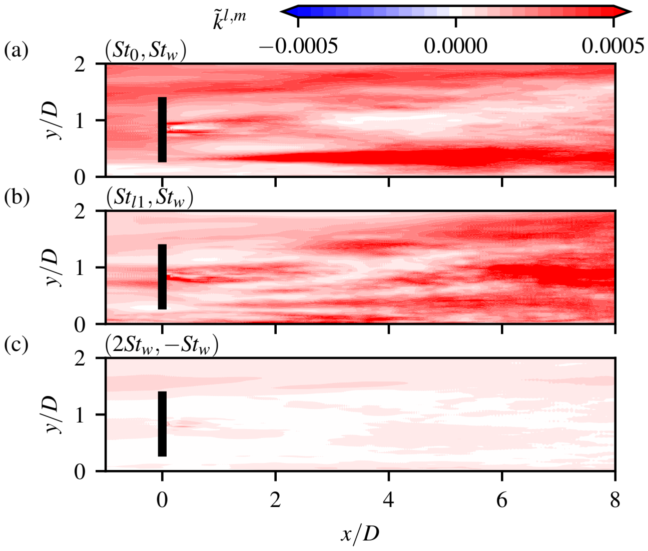

Figure 7: Contours of SSETM scale-specific coherent kinetic energy of select interactions of the wake meandering mode for (a) mean-wake meandering sum-interaction (St_0, St_w), (b) upwind-wake meandering sum-interaction (St_{l1}, St_w), and (c) first harmonic-wake meandering difference-interaction $(2\,St_w, St_w)$.

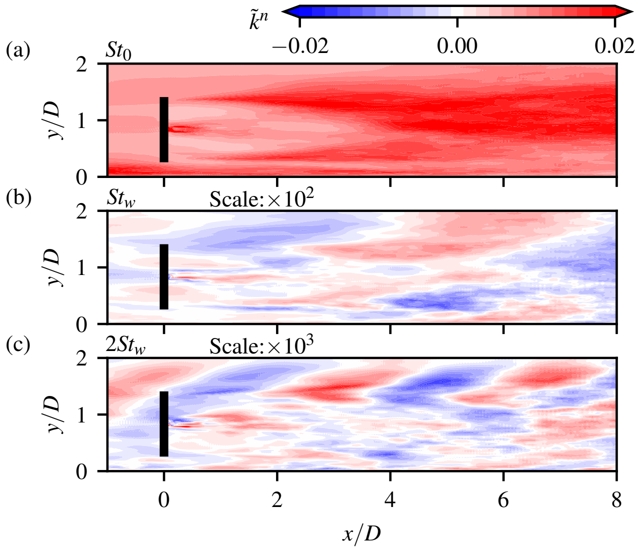

Figure 8: Contours of SSETM summed scale-specific coherent kinetic energy of (a) mean (St_0), (b) wake meandering (St_w), and (c) first harmonic of wake meandering $(2\,St_w)$ modes. Note the scale transformation in (b) and (c).

harmonics.

The sum of all scale interactions (both sum-interactions and difference-interactions) that correspond to the mean flow distortion (St_0) scale are shown as the summed scale-specific CKE in Fig. 8. This scale has the most CKE compared to all other scales in the flow, and due to this, the spatial distribution mirrors that of the TKE shown in Fig. 2(b). There is high energy near the hub vortex in the near wake, along the top and bottom tip shear layers starting at the rotor, and in the far wake due to wake meandering. Figures 8(b) and 8(c) show the summed scale-specific CKE for the wake meandering (St_w) and first harmonic of the wake meandering $(2\,St_w)$, respectively. There is significantly less CKE in the scale compared to that of the mean flow, however, the wake meandering scale accounts for the second most CKE after St_0. The CKE in wake meandering, shows a patterned oscillation that is expected from the wave-like pattern of wake meandering. The first harmonic shows similar patterns with a higher wavenumber. The peak CKE in wake meandering is at the top-tip position around $x/D = 4$, where TKE peaks and wake meandering oscillations are observed to be strongest.

Now, we focus on the spatial distribution of BMD bispectral modes of the streamwise velocity. These quantify the interaction of two scales where one of the scales is the wake meandering scale. Note that these calculate a mode field corresponding to the streamwise velocity and not the CKE identified in SSETM. This provides a complementary view of how scales interact with each other. Figure 9(a) shows the sum-interaction of the upwind scale St_{l1} and wake meandering St_w, similar to Fig. 7(b). The mode is distributed with the wave-like oscillation with a wavenumber similar to Fig. 8(b). The interaction is highest in the top-tip shear layer peaking in the far wake. This corroborates the scale-specific CKE of the interaction where CKE peaks in the far wake. The mode suggests that the upwind scale and wake meandering interact in the shear layer and energy is transported into the wake, which helps explain high CKE of this interaction throughout the far wake. Figure 9(b) shows the self sum-interaction of the wake meandering mode. Note that the sum of this interaction creates the first harmonic of wake meandering. This interaction represents a significant portion of total CKE in the first harmonic, which is corroborated by SSETM. The spatial distribution is similar to the summed scale-specific CKE of the first harmonic in Fig. 8(c), especially with a similar wavenumber. Finally, we look at an interaction that is only captured by the BMD and shown in the bispectrum in Fig. 6(a), the interaction of the mean flow and blade frequency. The spatial distribution is only nonzero around the rotor and does not appear downwind. Any sum-interaction between the blade frequency and wake meandering frequency is significantly smaller than this interaction.

The BMD cross-frequency field shows the “cause” of the interactions compared to the “effect” shown by the bispectral modes in Fig. 9. Figure 10(a) shows the cross frequency field corresponding to the interaction of the upwind scale and wake meandering scale. The cross frequency shows a similar spatial distribution that identifies the peak interaction in the top-tip shear layer. However, it also demonstrates that the far wake is affected by the interaction. Figure 10(b) is the cross-frequency field of

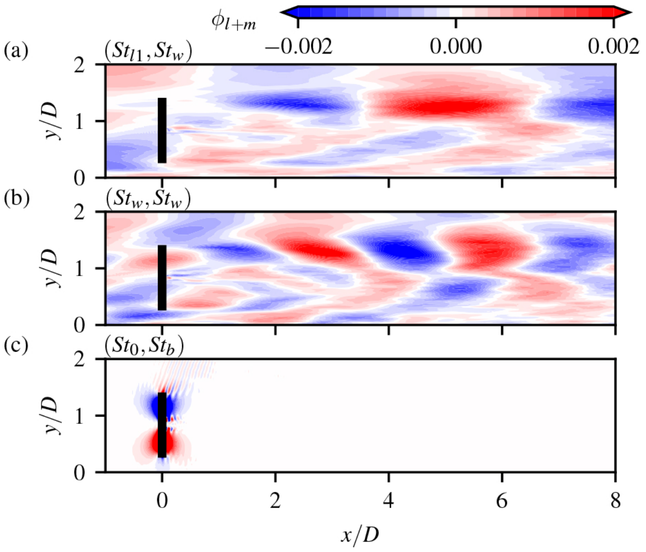

Figure 9: Contours of the BMD bispectral mode ϕ^{l+m} streamwise velocity component of select interactions related to wake meandering (a) upwind-wake meandering sum-interaction (St_{l1}, St_w), (b) self wake meandering sum-interaction (St_w, St_w), and (c) mean-blade sum-interaction (St_0, St_b).

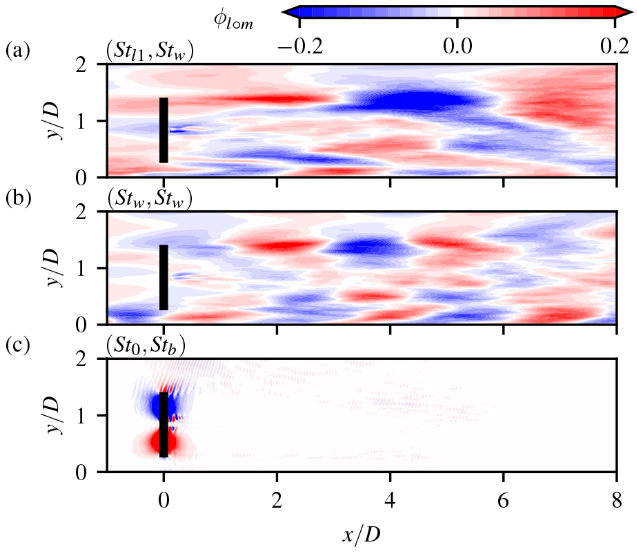

Figure 10: Contours of the BMD cross-frequency field $\phi^{l\circ m}$ streamwise velocity component of select interactions related to wake meandering for (a) upwind-wake meandering sum-interaction (St_{l1}, St_w), (b) self wake meandering sum-interaction (St_w, St_w), and (c) mean-blade sum-interaction (St_0, St_b).

the wake meandering self-interaction and shows the peak interactions occur in the shear layer of the wake. The cross-frequency field of the mean flow and blade frequency where the interaction is only observed near the rotor.

5. Conclusion

Wake meandering has a dominant effect on the dynamics of a wind turbine wake, but is just one of many frequency scales that are present. Scales interact in triads under the sum-zero condition. While the interactions are difficult to examine under commonly used spectral analyses of the power spectral density, they are fundamental in energy transfer in turbulent flows. Bispectral analyses offer a new tool to understand the scale interactions. We presented two different analyses that are based on modal decomposition to address the multi-dimensionality of the data. The first is the method developed through DMD and the triple decomposition of turbulence (SSETM), which quantifies the kinetic energy and energy transfer and transport of specific scale interactions. The second is a method based on the bispectral density, which uses correlations between three frequencies to identify triads (BMD). Both methods produced a bispectrum of frequencies of a utility wind turbine in a boundary layer. Upwind, rotor, and downwind dominant frequencies were identified by the spectral analyses. All were able to identify low upwind frequencies and far wake meandering. These interactions were the most dominant and shown to contain significant amount of energy. While the SSETM was able to quantify the kinetic energy related to triadic interactions, the BMD was able to quantify modes and cross-frequency fields showing how scales interact. Both corroborated evidence of the effects of upwind scales on wake meandering and how higher-order harmonics of the wake meandering frequency are produced. Identifying the effects of rotor frequency scales on wake meandering proved to be more difficult as those interactions were not shown to be as significant compared to upwind or self wake meandering interactions. Further work will seek to enhance on identification and data reduction and quantify energy transfer to elucidate cause-and-effects of wake meandering.

Acknowledgments

This work supported by the National Science Foundation under Grant No. 21-36371. This work used Anvil at Purdue University through allocation PHY220038 from the Advanced Cyberinfrastructure Coordination Ecosystem: Services & Support (ACCESS) program, which is supported by National Science Foundation Grants No. 21-38259, No. 21-38286, No. 21-38307, No. 21-37603, and No. 21-38296.

Appendix A. Statistical Convergence

Obtaining statistical convergence of the velocity is a challenge due to the long time averaging intervals that are necessary. The power spectral density requires the second moment of the velocity to be converged, while the bispectral density requires the third moment or skewness to be converged. Time averaging of the LES was performed over almost 1000 turbine rotation periods, which is over a considerably longer time period compared to other studies [27, 51]. Figure A.11 shows the effect of time averaging over a time interval equal to tT_0, where T_0 is the initial time, of the mean velocity components U, velocity variances $\overline{uu}$, and the skewness of the velocity components $\overline{uuu}$. The variance and skewness are normalized by the upwind friction velocity u_τ. The convergence study is shown for four locations downwind of the rotor at hub height along the centerline. Each component of each statistic shows that a final converged statistic is reached before the end of the time averaging period.

Appendix A. Bispectral Method Convergence

The convergence of the bispectral methods for both cases is based on the parameters and tolerances of the algorithms and the amount of data retained from the snapshots. For SSETM the most dominant effect on the bispectrum in terms of convergence and the accuracy is number of modes retained for DMD both from the SVD regularization and the sparsity promoting DMD. Figure A.12 shows the convergence of the summed bispectrum, which is the some of all frequency pairs that equal the third frequency as defined in Eq. (8). As the number of modes is reduced, the high frequency modes begin to diverge. However, in our analysis, we focus only on the low frequency modes, which are the same for each case. For the BMD, the convergence is based on the number of realizations N_{blk} that are employed. Figure A.13 shows the convergence of BMD method for different number of realizations. All tolerances used in the methods are based on relative errors less than 1×10^{-8}.

References

[1] S. Ivanell, R. Mikkelsen, J. N. Sørensen, D. Henningson, Stability analysis of the tip vortices of a wind turbine, Wind Energy 13 (8) (2010) 705–715.

[2] S. Sarmast, R. Dadfar, R. F. Mikkelsen, P. Schlatter, S. Ivanell, J. N. Sørensen, D. S. Henningson, Mutual inductance instability of the tip vortices behind a wind turbine, Journal of Fluid Mechanics 755 (2014) 705–731.

[3] D. Foti, X. Yang, M. Guala, F. Sotiropoulos, Wake meandering statistics of a model wind turbine: Insights gained by large eddy simulations, Physical Review Fluids 1 (4) (2016) 044407.

[4] M. Abkar, F. Porté-Agel, Influence of atmospheric stability on wind-turbine wakes: A large-eddy simulation study, Physics of Fluids 27 (3) (2015) 035104.

[5] D. Foti, X. Yang, L. Shen, F. Sotiropoulos, Effect of wind turbine nacelle on turbine wake dynamics in large wind farms, Journal of Fluid Mechanics 869 (2019) 1–26.

[6] A. Clifton, A. Smith, M. Fields, Wind plant preconstruction energy estimates. current practice and opportunities, Tech. rep., National Renewable Energy Lab.(NREL), Golden, CO (United States) (2016).

[7] Ørsted presents update on its long-term financial targets, Ørsted Company Announcement List (2019).
URL `https://orsted.com/en/Company-Announcement-List/2019/10/1937002`

[8] B. Panjwani, M. Kvittem, L. Eliassen, H. Ormberg, M. Godvik, Effect of wake meandering on aeroelastic response of a wind turbine placed in a park, in: Journal of Physics: Conference Series, Vol. 1356, IOP Publishing, 2019, p. 012039.

[9] H. A. Madsen, G. C. Larsen, T. J. Larsen, N. Troldborg, R. Mikkelsen, Calibration and validation of the dynamic wake meandering model for implementation in an aeroelastic code, Journal of Solar Energy Engineering 132 (4) (2010).

[10] G. C. Larsen, H. A. Madsen, K. Thomsen, T. J. Larsen, Wake meandering: a pragmatic approach, Wind Energy: An International Journal for Progress and Applications in Wind Power Conversion Technology 11 (4) (2008) 377–395.

[11] D. Medici, P. Alfredsson, Measurements on a wind turbine wake: 3D effects and bluff body vortex shedding, Wind Energy 9 (3) (2006) 219–236.

[12] R. H. Kraichnan, Inertial ranges in two-dimensional turbulence, The Physics of Fluids 10 (7) (1967) 1417–1423.

[13] R. H. Kraichnan, Inertial-range transfer in two-and three-dimensional turbulence, Journal of Fluid Mechanics 47 (3) (1971) 525–535.

[14] F. Waleffe, On a self-sustaining process in shear flows, Physics of Fluids 9 (4) (1997) 883–900.

[15] J. A. Domaradzki, R. S. Rogallo, Local energy transfer and nonlocal interactions in homogeneous, isotropic turbulence, Physics of Fluids A: Fluid Dynamics 2 (3) (1990) 413–426.

[16] J. G. Brasseur, C.-H. Wei, Interscale dynamics and local isotropy in high reynolds number turbulence within triadic interactions, Physics of Fluids 6 (2) (1994) 842–870.

[17] J. A. Domaradzki, W. Liu, C. Härtel, L. Kleiser, Energy transfer in numerically simulated wall-bounded turbulent flows, Physics of Fluids 6 (4) (1994) 1583–1599.

[18] K. Lii, M. Rosenblatt, C. Van Atta, Bispectral measurements in turbulence, Journal of Fluid Mechanics 77 (1) (1976) 45–62.

[19] T. Corke, F. Shakib, H. Nagib, Mode selection and resonant phase locking in unstable axisymmetric jets, Journal of Fluid Mechanics 223 (1991) 253–311.

[20] K. L. Gee, A. A. Atchley, L. E. Falco, M. R. Shepherd, L. S. Ukeiley, B. J. Jansen, J. M. Seiner, Bicoherence analysis of model-scale jet noise, The Journal of the Acoustical Society of America 128 (5) (2010) EL211–EL216.

[21] L. Sirovich, Turbulence and the dynamics of coherent structures. I. coherent structures, Quarterly of Applied Mathematics 45 (3) (1987) 561–571.

[22] C. VerHulst, C. Meneveau, Altering kinetic energy entrainment in large eddy simulations of large wind farms using unconventional wind turbine actuator forcing, Energies 8 (1) (2015) 370–386.

[23] D. Foti, S. Giorno, K. Duraisamy, An adaptive mesh refinement approach based on optimal sparse sensing, Theoretical and Computational Fluid Dynamics 34 (4) (2020) 457–482.

[24] P. J. Schmid, Dynamic mode decomposition of numerical and experimental data, Journal of Fluid Mechanics 656 (2010) 5–28.

[25] A. Towne, O. T. Schmidt, T. Colonius, Spectral proper orthogonal decomposition and its relationship to dynamic mode decomposition and resolvent analysis, Journal of Fluid Mechanics 847 (2018) 821–867.

[26] I. Mezić, Analysis of fluid flows via spectral properties of the Koopman operator, Annual Review of Fluid Mechanics 45 (2013) 357–378.

[27] D. Foti, X. Yang, F. Campagnolo, D. Maniaci, F. Sotiropoulos, Wake meandering of a model wind turbine operating in two different regimes, Phys. Rev. Fluids 3 (5) (2018) 054607.

[28] Z. Li, X. Yang, Evaluation of actuator disk model relative to actuator surface model for predicting utility-scale wind turbine wakes, Energies 13 (14) (2020) 3574.

[29] O. T. Schmidt, Bispectral mode decomposition of nonlinear flows, Nonlinear Dynamics 102 (4) (2020) 2479–2501.

[30] D. K. Kinjangi, D. Foti, Characterization of energy transfer and triadic interactions of coherent structures in turbulent wakes, Journal of Fluid Mechanics 971 (2023) A7.

[31] F. Waleffe, The nature of triad interactions in homogeneous turbulence, Physics of Fluids A: Fluid Dynamics 4 (2) (1992) 350–363.

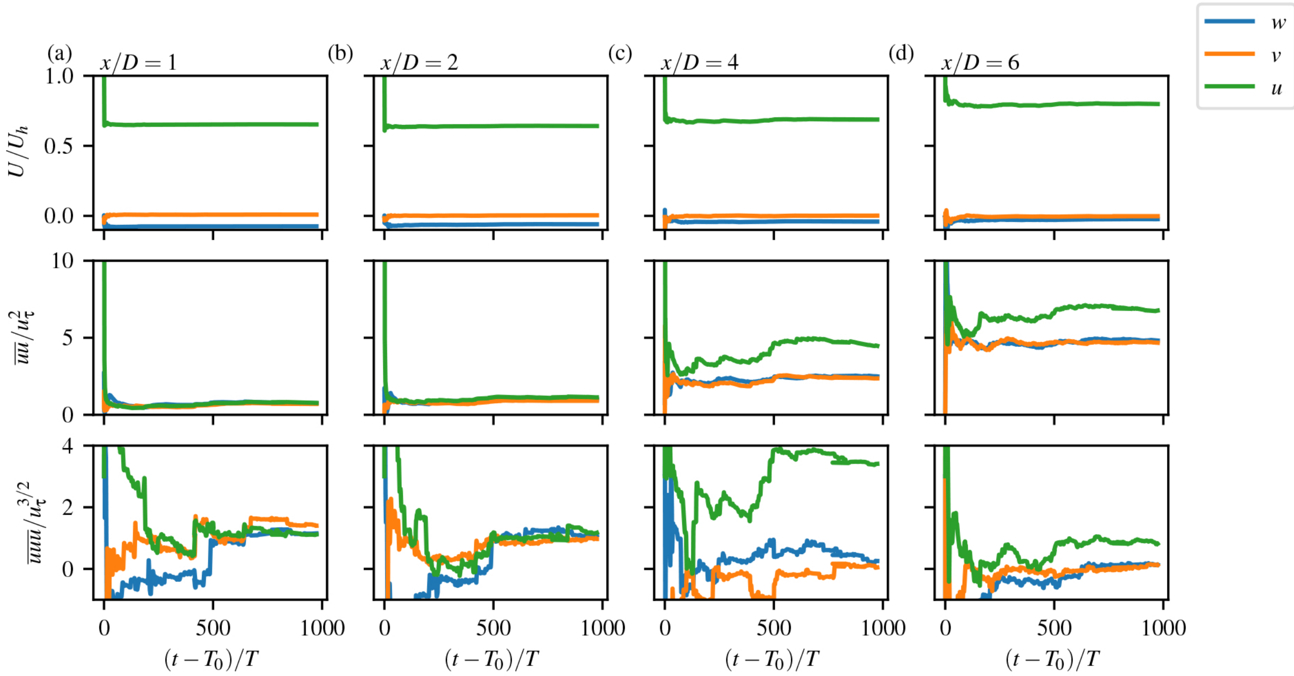

Figure A.11: The effect of averaging over times $t - T_0$ for the mean, variance, and skewness of each velocity component.

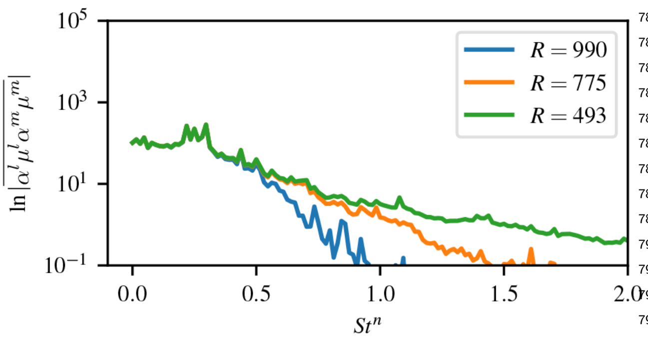

Figure A.12: Convergence of the summed bispectrum for the SSETM method for various number of modes retained.

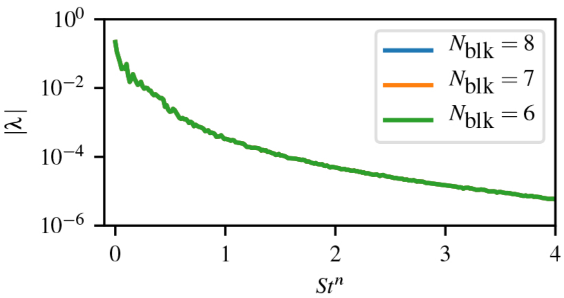

Figure A.13: Convergence of the summed bispectrum for the BMD method for various realizations.

[32] M. R. Jovanović, P. J. Schmid, J. W. Nichols, Sparsity-promoting dynamic mode decomposition, Physics of Fluids 26 (2) (2014) 024103.

[33] C. He, G. Watson, An algorithm for computing the numerical radius, IMA Journal of Numerical Analysis 17 (3) (1997) 329–342.

[34] X. Yang, F. Sotiropoulos, R. J. Conzemius, J. N. Wachtler, M. B. Strong, Large-eddy simulation of turbulent flow past wind turbines/farms: the Virtual Wind Simulator (VWiS), Wind Energy 18 (12) (2015) 2025–2045.

[35] L. Ge, F. Sotiropoulos, A numerical method for solving the 3D unsteady incompressible Navier–Stokes equations in curvilinear domains with complex immersed boundaries, Journal of Computational Physics 225 (2) (2007) 1782–1809.

[36] J. Smagorinsky, General circulation experiments with the primitive equations: I. the basic experiment, Monthly Weather Review 91 (3) (1963) 99–164.

[37] M. Germano, U. Piomelli, P. Moin, W. H. Cabot, A dynamic subgrid-scale eddy viscosity model, Physics of Fluids A: Fluid Dynamics 3 (7) (1991) 1760–1765.

[38] D. K. Lilly, A proposed modification of the germano subgrid-scale closure method, Physics of Fluids A: Fluid Dynamics 4 (3) (1992) 633–635.

[39] W. Z. Shen, J. N. Sørensen, J. Zhang, Actuator surface model for wind turbine flow computations, in: 2007 European Wind Energy Conference & Exhibition, 2007.

[40] X. Yang, X. Zhang, Z. Li, G.-W. He, A smoothing technique for discrete delta functions with application to immersed boundary method in moving boundary simulations, J. Comput. Phys. 228 (20) (2009) 7821–7836.

[41] Z. Du, M. Selig, A 3-d stall-delay model for horizontal axis wind turbine performance prediction, in: 1998 ASME Wind Energy Symposium, 1998, p. 21.

[42] W. Z. Shen, R. Mikkelsen, J. N. Sørensen, C. Bak, Tip loss corrections for wind turbine computations, Wind Energy 8 (4) (2005) 457–475.

[43] X. Yang, F. Sotiropoulos, A new class of actuator surface models for wind turbines, Wind Energy 21 (5) (2018) 285–302.

[44] M. Uhlmann, An immersed boundary method with direct forcing for the simulation of particulate flows, J. Comput. Phys. 209 (2) (2005) 448–476.

[45] H. Schlichting, K. Gersten, Boundary-Layer Theory, Springer Science & Business Media, 2003.

[46] X. Yang, J. Hong, M. Barone, F. Sotiropoulos, Coherent dynamics in the rotor tip shear layer of utility-scale wind turbines, Journal of Fluid Mechanics 804 (2016) 90–115. doi:10.1017/jfm.2016.503.

[47] D. Foti, X. Yang, F. Sotiropoulos, Similarity of wake meandering for different wind turbine designs for different scales, Journal of Fluid Mechanics 842 (2018) 5–25.

[48] M. Guala, S. Hommema, R. Adrian, Large-scale and very-large-scale motions in turbulent pipe flow, Journal of Fluid Mechanics 554 (2006) 521–542.

[49] R. J. Adrian, Hairpin vortex organization in wall turbulence, Physics of Fluids 19 (4) (2007) 041301.

[50] D. Foti, Coherent vorticity dynamics and dissipation in a utility-scale wind turbine wake with uniform inflow, Theoretical and Applied Mechanics Letters 11 (5) (2021) 100292.

[51] X. Yang, K. B. Howard, M. Guala, F. Sotiropoulos, Effects of a three-dimensional hill on the wake characteristics of a model wind turbine, Physics of Fluids 27 (2) (2015) 025103.

[52] M. Guala, M. Metzger, B. J. McKeon, Interactions within the turbulent boundary layer at high Reynolds number, Journal of Fluid Mechanics 666 (2011) 573–604.

[53] A. Qatramez, D. Foti, Reduced-order model predictions of wind turbines via mode decomposition and sparse sampling, in: AIAA Scitech 2021 Forum, 2021, p. 1602.

[54] D. Medici, P. H. Alfredsson, Measurements behind model wind turbines: further evidence of wake meandering, Wind Energy 11 (2) (2008) 211–217.

[55] L. Chamorro, C. Hill, S. Morton, C. Ellis, R. Arndt, F. Sotiropoulos, On the interaction between a turbulent open channel flow and an axial-flow turbine, Journal of Fluid Mechanics 716 (2013) 658–670.

[56] V. L. Okulov, I. V. Naumov, R. F. Mikkelsen, I. K. Kabardin, J. N. Sørensen, A regular strouhal number for large-scale instability in the far wake of a rotor, Journal of Fluid Mechanics 747 (2014) 369–380.

[57] K. B. Howard, A. Singh, F. Sotiropoulos, M. Guala, On the statistics of wind turbine wake meandering: An experimental investigation, Physics of Fluids 27 (7) (2015) 075103.